

# NEW LIMITS ON GAMMA-RAY EMISSION FROM GALAXY CLUSTERS

RHIANNON D. GRIFFIN<sup>1</sup>, XINYU DAI<sup>1</sup>, CHRISTOPHER S. KOCHANÉK<sup>2</sup>

*Submitted to ApJ*

## ABSTRACT

Galaxy clusters are predicted to produce  $\gamma$ -rays through cosmic ray interactions and/or dark matter annihilation, potentially detectable by the *Fermi* Large Area Telescope (*Fermi*-LAT). We present a new, independent stacking analysis of *Fermi*-LAT photon count maps using the 78 richest nearby clusters ( $z < 0.12$ ) from the Two Micron All-Sky Survey (2MASS) cluster catalog. We obtain the lowest limit on the photon flux to date,  $2.3 \times 10^{-11}$  phot cm<sup>-2</sup> s<sup>-1</sup> (95% confidence) per cluster in the 0.8–100 GeV band, which corresponds to a luminosity limit of  $3.5 \times 10^{44}$  phot s<sup>-1</sup>. We also constrain the emission limits in a range of narrower energy bands. Scaling to recent cosmic ray acceleration and  $\gamma$ -ray emission models, we find that cosmic rays represent a negligible contribution to the intra-cluster energy density and gas pressure.

*Subject headings:* acceleration of particles — galaxies: clusters: general — galaxies: clusters: intra-cluster medium — gamma rays: galaxies: clusters

## 1. INTRODUCTION

Galaxy clusters are the largest gravitationally bound structures in the universe and as such are important tools for studies of structure formation and cosmology. Past and current methods of detection include optical and X-ray observations, the Sunyaev-Zeldovich effect, and gravitational lensing (e.g., Kravtsov & Borgani 2012 and references within). Each new way of observing galaxy clusters can reveal more about these objects, the physics involved, and the history of their formation.

The prevailing structure formation theory suggests that galaxy clusters formed through the hierarchical merging of smaller systems, driven by the gravity of the dominant dark matter. During the merging process, merger shocks form in the baryons, accelerating cosmic ray (CR) particles to ultra-relativistic speeds with Lorentz factors  $\Gamma \gg 1000$  (e.g., Völk et al. 1996; Berezhinsky et al. 1997). Evidence for this can be seen in the form of cluster radio halos or relics, spatially extended radio emission or giant radio arcs on scales of  $\sim 1$  Mpc due to synchrotron emission by CR electrons (Feretti et al. 2012). Electrons lose energy quickly ( $\leq 10^8$  yr) due to the high efficiency of synchrotron emission, non-thermal bremsstrahlung, and up-scattering of CMB radiation and so radio relics only probe recent events.

The shock models also predict that a much larger amount of energy is deposited in the hadronic component (ultra-relativistic protons). CR protons have a very long cooling time ( $\geq 10^{10}$  yr) and interact with protons in the hot intergalactic medium (1–10 keV) of the clusters (e.g., Berezhinsky et al. 1997; Berrington & Dermer 2003; Kravtsov & Borgani 2012). Hadronic debris from these p–p interactions includes neutral pions, whose main decay channel is two  $\gamma$ -rays:  $\pi^0 \rightarrow 2\gamma$  (99%)

(Amsler et al. 2008). This  $\pi^0$  decay is expected to dominate the CR induced  $\gamma$ -ray emission which is predicted to be detectable by the *Fermi* Large Area Telescope and other  $\gamma$ -ray missions (*Fermi*-LAT, e.g., Ackermann et al. 2013; Vazza & Brüggen 2014; Reimer et al. 2003; Aleksić et al. 2012; Arlen et al. 2012).

Other processes that contribute to the  $\gamma$ -ray emission are inverse Compton scattering and relativistic bremsstrahlung emissions, but these are likely subdominant (e.g., Jeltema et al. 2009; Pinzke & Frommer 2010; Vazza & Brüggen 2014; Brunetti & Jones 2014). In addition, to detect any dark matter annihilation signal in clusters and set stringent constraints on dark matter annihilation cross-sections, the CR emission is a background that must be characterized as part of the spectrum (Ackermann et al. 2013; Huber et al. 2013).

Several recent papers focus on *Fermi*-LAT searches for this  $\gamma$ -ray emission; however, no diffuse  $\gamma$ -ray emission from galaxy clusters has firmly been detected (Ackermann et al. 2014, Huber et al. 2013, Prokhorov and Churazov 2014 by stacking  $\sim 50$  clusters; Ackermann et al. 2014, Han et al. 2012, Zandanel and Ando 2014 for individual clusters). *Fermi*-LAT has detected point-like  $\gamma$ -ray emission from the radio galaxies at the centers of the Virgo and Perseus clusters, although these are not attributed to neutral pion decay in the intergalactic medium (Abdo et al. 2009a, 2009b). In these studies, extragalactic sources beyond the 2FGL catalog<sup>3</sup> (Nolan et al. 2012) could cause contamination (Han et al. 2012, Ackermann et al. 2014, Prokhorov and Churazov 2014). The results of the stacking analyses of Ackermann et al. (2014), Huber et al. (2013), and Prokhorov and Churazov (2014) establish the lowest flux upper limits to date and Huber et al. (2013) reached the lowest limits at  $2.8\text{--}4.9 \times 10^{-11}$  phot cm<sup>-2</sup> s<sup>-1</sup> in the 1–300 GeV band. Flux upper limits from these stacking analyses are in partial conflict with current models of CR acceleration (e.g., Huber et al. 2013). Vazza & Brüggen (2014) argued that the expected  $\gamma$ -ray emission for most clusters with

<sup>1</sup> Homer L. Dodge Department of Physics and Astronomy, University of Oklahoma, Norman, OK, 73019; Rhiannon.D.Griffin-1@ou.edu, xdai@ou.edu

<sup>2</sup> Department of Astronomy and the Center for Cosmology and Astroparticle Physics, Ohio State University, Columbus, OH 43210; kochanek@astronomy.ohio-state.edu

<sup>3</sup> <http://heasarc.gsfc.nasa.gov/W3Browse/all/fermilpsc.html>

radio relics should be close to or above the flux limits set by these stacking analyses.

In this Letter, we present an independent study on this topic, using a uniformly selected sample of nearby clusters. Our sample is unique among *Fermi* cluster stacking analyses as all of the studies mentioned above use only high X-ray flux HIFLUGCS clusters (Reiprich & Böhringer 2002). Our final selection of 78 clusters includes just 5 HIFLUGCS clusters and of the original 162, 33 are in the HIFLUGCS catalog. In §2 we discuss the cluster sample, the  $\gamma$ -ray data reduction process and the stacking analysis, and we discuss the results and consequences in §3. We assume  $H_0 = 70 \text{ km s}^{-1} \text{ Mpc}^{-1}$ ,  $k = 0$ ,  $\Omega_M = 0.3$ , and  $\Omega_\Lambda = 0.7$ .

## 2. ANALYSIS

Our cluster sample consists of the richest, nearby ( $z < 0.12$ ) clusters in the 2MASS catalog of clusters identified using a matched filter algorithm (Kochanek et al. 2003). Like *Fermi*, 2MASS is also an all-sky survey, and we start with the 162 richest clusters outside of the Galactic plane ( $|b| > 20^\circ$ ) with  $z < 0.12$  ( $\bar{z} = 0.08$ ) and typical masses of  $M_{200} \sim 6 \times 10^{14} M_\odot$ . The sample is well-characterized in richness and distance with extensive calibrations using both near-IR and X-ray stacking analyses (Dai et al. 2007; Dai et al. 2010; Blackburne & Kochanek 2012). We eventually use 78 of the original 162 clusters as discussed in §3. Details of these clusters are listed in Table 1.

We downloaded the Pass 7 LAT data from the Fermi Science Support Center (FSSC)<sup>4</sup>, along with the Fermi Science Tools (version v9r31p1). We used the pre-generated weekly all-sky files which span 2008–08–04 to 2013–06–20 for a total of 255 weeks ( $\sim 5$  years) for SOURCE class photon events. We followed the FSSC Data Preparation recommendations for our analysis. Since the point spread function (PSF) of *Fermi*-LAT decreases with energy, we used a minimum energy threshold of  $\sim 1 \text{ GeV}$  so that the PSF is always more compact than  $0.6 \text{ deg}$ , which also lowers the contributions of point sources. A zenith angle cut of  $100^\circ$  was applied to avoid CR-produced  $\gamma$ -rays originating from the Earth’s atmospheric limb. Good time intervals were identified using the recommended selection expression `((DATA_QUAL==1) && (LAT_CONGIF==1) && ABS(ROCK_ANGLE)<52)` to exclude periods of dead time during spacecraft maneuvers, software updates, and transits through the Southern Atlantic Anomaly.

We first extracted count and exposure maps for each week and then stacked them in time to make a single count and exposure map for each cluster. We then stacked the clusters to obtain the final stacked image. As we generate the map for each cluster, we search for high background flares from variable  $\gamma$ -ray sources in the weekly images,  $2\sigma$  above the mean photon flux ( $\text{phot cm}^{-2} \text{ s}^{-1}$ ), and reject these time periods. We used seven logarithmically spaced energy bins to cover the  $0.8 - 100 \text{ GeV}$  band and the exposure maps were calculated at the mean energy of each bin.

Since clusters at higher redshifts have smaller angular sizes, we combine the clusters over a fixed  $20 \text{ Mpc}$  radius region of interest (ROI) binned into  $2 \text{ Mpc}$  pixels.

This is more physical than stacking on a fixed angular scale as done previously (Ackermann et al. 2013; Huber et al. 2013; Prokhorov & Churazov 2013). The cluster emission should lie only in the central  $2 \text{ Mpc}$  and the remainder provides the background region. We also weight the clusters by  $z^2$  so that the stacked signal is not dominated by nearby clusters. This also helps to reduce the variance in the final, stacked image. Since the  $2 \text{ Mpc}$  extraction region can be smaller than the *Fermi* PSFs at lowest energies  $\sim 1 \text{ GeV}$ , we calculated energy-dependent aperture flux corrections, and applied them to the flux limits calculated in all energy bands.

We masked bright sources from the 2FGL catalog (Nolan et al. 2012) using  $0.5$  radius circles to minimize contributions from known point sources to the background. This mask radius is larger than the PSF of point sources for all but the lowest energies ( $\sim 1 \text{ GeV}$ ) considered in our analysis. We tested various mask sizes and found that  $0.5$  radius resulted in the smoothest background, although there is still some contamination to the background, up to 35% of the source signal. This contamination contributes randomly to the background and has little effect on the final flux estimates. The masked region was then statistically filled using the average local background, which we defined to be the annulus with inner and outer radii of  $0.7$  and  $0.9$ , respectively. This average local background contains little contamination from the bright source itself ( $< 8\%$  of the source signal). For multiple bright sources, we masked from brightest to dimmest to minimize the contamination on adjacent masks. We then visually rejected clusters with poorly masked, bright 2FGL sources. We flattened each count map to the average exposure near the center of each cluster to make the effective exposure time uniform across the image. For any overlapping clusters (separation  $< 2 \text{ Mpc}$ ) we excluded the more distant cluster. We also excluded one cluster where a bright source mask completely covers the cluster region. These procedures left us with 78 clusters (Figure 1, left) with the final stacked  $0.8 - 100 \text{ GeV}$  image shown in Figure 1 (right). In addition to this map we also examined maps in which we sequentially stack the clusters in order of increasing background variance. This “stacking by variance” method provides an alternate approach for images with complex, multi-component backgrounds including bright sources, the Galactic background, and the diffuse extragalactic background.

## 3. RESULTS AND DISCUSSION

Within our  $2 \text{ Mpc}$  source region of the final stack of 78 count maps (see Figure 1, right) we detect no excess  $\gamma$ -ray emission above the background. We find an aperture corrected 95% confidence upper limit of  $2.48 \times 10^{-11} \text{ phot cm}^{-2} \text{ s}^{-1}$  per cluster in the  $0.8 - 100 \text{ GeV}$  band when we compare the source region to 500 random  $2 \text{ Mpc}$  regions in our standard background annulus ( $3 - 19 \text{ Mpc}$ ). This Monte-Carlo approach is more general in that it does not assume a Poisson background. The choice of the outer background radius has little effect (see Figure 2). Figure 2 also shows how the limits depend on the number of clusters as we stack them in order of increasing variance. There is an initial, rapid decline and then a flattening with a minimum at  $N = 45 - 55$  clusters. Taking the median of the best upper limits

<sup>4</sup> <http://fermi.gsfc.nasa.gov/ssc>

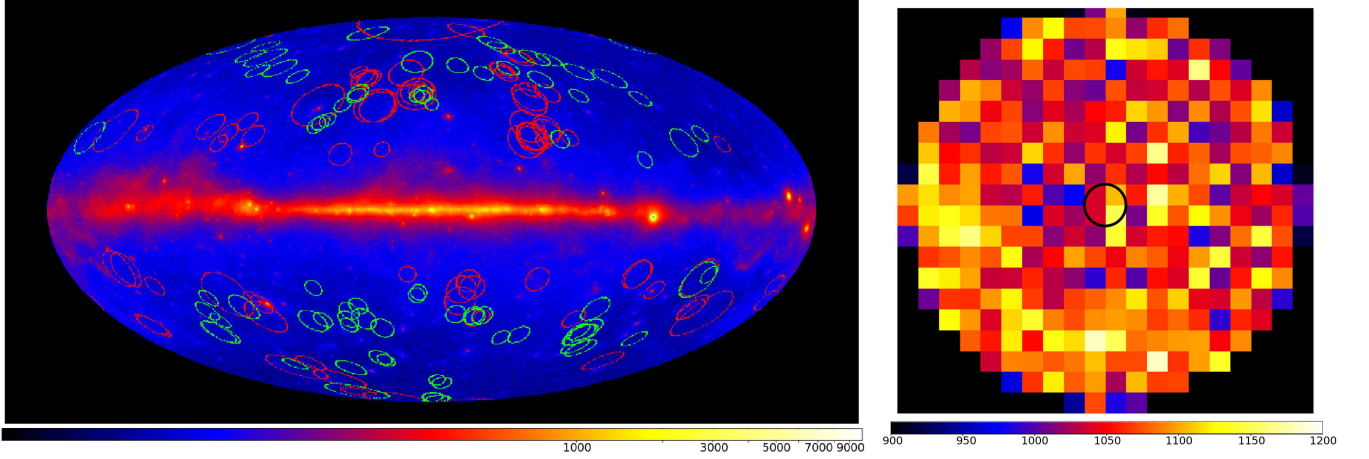


FIG. 1.— (Left) All-sky photon count map for the analyzed data. The green ellipses show the locations and area of the 78 rich 2MASS clusters included in the final analysis and red ellipses show the rejected clusters. (Right) Final 0.8–100 GeV stacked image for the 78 clusters. The analysis region is 20 Mpc in radius and we limit the flux in the central 2 Mpc source region (black circle).

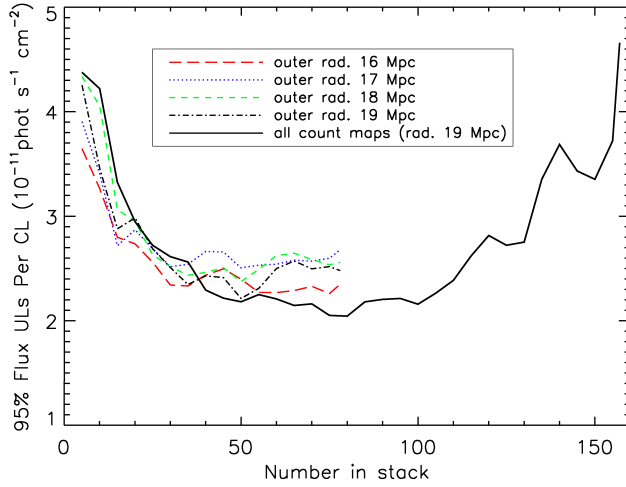


FIG. 2.— Photon flux upper limits [0.8–100 GeV] per cluster as a function of the number of clusters included in the stack for different outer background radii (the inner radius is fixed at 3 Mpc). The stacks are ordered by the increasing variance of the cluster maps. The limits initially decline and then flatten. The black solid line indicates the stacking analysis that includes all count maps not in the Galactic plane, even those with poorly masked 2FGL sources. The trend increases after  $N \sim 100$  suggesting that we correctly rejected images with large contamination.

from the stacking by variance method from the four different background apertures, we obtain the final upper limit of  $2.32 \times 10^{-11}$  phot cm $^{-2}$  s $^{-1}$  per cluster corresponding to a luminosity limit of  $3.5 \times 10^{44}$  phot s $^{-1}$  in the 0.8–100 GeV band given the median redshift of  $z = 0.0758$ . If we extend this to include clusters with poorly masked 2FGL sources (black, solid line in Figure 2), the number of clusters increases to 155 but the limits begin to significantly worsen as we reach  $N > 100$  clusters. This indicates that our exclusion of these clusters was well-justified. We also constrain the  $\gamma$ -ray emission upper limits in a range of narrower energy bands and these limits are listed in Table 2.

Figure 3 compares our aperture corrected 95% confidence limits for the 0.8–100 GeV band to the results of Ackermann et al. (2014) (1–200 GeV) and

TABLE 1  
GALAXY CLUSTER SAMPLE

Name	RA	Decl	$z$	Richness
2MASSCL J0330–5235	52.590	–52.585	0.060	28.758
2MASSCL J0317–4417	49.438	–44.297	0.074	13.183
2MASSCL J0108–1526	17.228	–15.435	0.053	10.392
2MASSCL J0327–5323	51.841	–53.392	0.061	16.375
2MASSCL J0343–5338	55.753	–53.643	0.059	20.109
2MASSCL J0312–4725	48.191	–47.417	0.081	10.006
2MASSCL J2235+0129	338.935	1.496	0.059	14.214
2MASSCL J0112+1611	18.103	16.196	0.061	11.029
2MASSCL J0544–2558	86.200	–25.968	0.042	15.188
2MASSCL J1311+3915	197.832	39.262	0.072	15.287

NOTE. — Position, redshift and richness for the 78 galaxy clusters used in the final stacked image, where the richness is the number of galaxies with luminosity  $L > L_*$  (Kochanek et al. 2003). The clusters are ordered by the variance of the background, starting with the lowest variance cluster. Note that 5 of the 78 clusters in our final stack are HIFLUGCS clusters (Reiprich & Böhringer 2002). Table 1 is published in its entirety in the electronic edition of the *Astrophysical Journal*. A portion is shown here for guidance regarding its form and content.

Huber et al. (2013) (1–300 GeV). We corrected for energy band differences by modeling the photon flux as  $dN/dE \propto (E/E_0)^{-2}$  (Pfrommer & Enßlin 2004; Huber et al. 2013), but the corrections are very small ( $\sim 5\%$ ). As seen in Figure 3, our new flux limits are an order of magnitude stronger than those for typical individual clusters and a factor of 2.1–1.2 improvement on the Huber et al. (2013) stacking limits of  $2.8$ – $4.9 \times 10^{-11}$  phot cm $^{-2}$  s $^{-1}$ . Because the Huber et al. (2013) sample is slightly closer, with a mean redshift of  $z = 0.052$ , this results in a factor two difference in  $z^2$  compared to our sample. The mean mass of the Huber et al. (2013) clusters is also roughly a factor of two larger at  $M_{500} = 5.6 \times 10^{14} M_\odot$ , thus our mass-weighted luminosity limit is twice that of Huber et al. (2013), but for slightly smaller systems. In the 10–300 GeV band, our mass-weighted luminosity limit is also consistent with the constraint from Prokhorov & Churazov (2014).

Gamma-ray emission from galaxy clusters probes the non-thermal component of the intra-cluster gas. We can compare our flux limits to recent model predictions

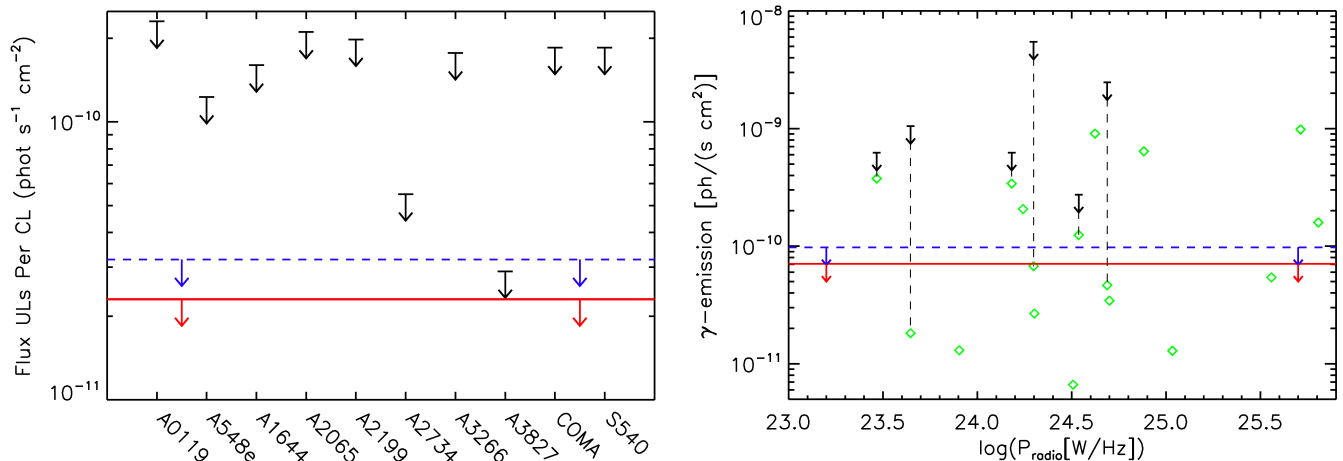


FIG. 3.— (Left) Flux limits from recent *Fermi*-LAT studies. The arrows are 10 clusters randomly selected from Ackermann et al. (2014). The lower red, solid line is our new upper limit, and the upper blue, dashed limit is from Huber et al. (2013). (Right) Model predictions for the 0.2–100 GeV flux for galaxy clusters with radio relics (green diamonds, from Vazza & Brüggen 2014) as compared to limits from individual cluster (black arrows, Ackermann et al. 2013) and the stacking limits from Huber et al. (2013, blue, dashed lines) and our analysis (red, solid line). We converted our 0.8–100 GeV limit to the 0.2–100 GeV band by scaling Vazza & Brüggen’s (2014) conversion of Huber et al. (2013) limits that assumed a proton energy index of 2. Notice that the flux limit derived from our stacking method is less than that found by Huber et al. (2013) and therefore the comparison of our upper limit can emphasize the problem described by Vazza & Brüggen (2014), where upper limits on  $\gamma$ -ray flux obtained from stacking methods are lower than the predicted fluxes from nearby clusters.

TABLE 2  
PHOTON FLUX UPPER LIMITS FROM STACKING ANALYSES OF  
GALAXY CLUSTERS

Energy Range	Outer Bkg. Radius	Flux UL ( $N \equiv 78$ )	Lowest UL ( $N$ )
0.8 – 100.0	16 Mpc	23.5	22.6 ( $N = 75$ )
13.0 – 300.0	16 Mpc	1.32	1.24 ( $N = 70$ )
0.8 – 1.6	16 Mpc	20.9	17.2 ( $N = 70$ )
1.6 – 3.2	16 Mpc	8.06	7.87 ( $N = 55$ )
3.2 – 6.3	16 Mpc	3.35	3.13 ( $N = 50$ )
6.3 – 13.0	16 Mpc	1.88	1.83 ( $N = 70$ )
13.0 – 25.0	16 Mpc	1.01	1.01 ( $N = 78$ )
25.0 – 50.0	16 Mpc	0.591	0.569 ( $N = 70$ )
50.0 – 100.0	16 Mpc	0.419	0.415 ( $N = 75$ )
100.0 – 170.0	16 Mpc	0.322	0.293 ( $N = 65$ )
170.0 – 300.0	16 Mpc	0.278	0.236 ( $N = 75$ )

NOTE. — Flux upper limits (UL) per cluster at 95% confidence in units of  $10^{-12} \text{phot cm}^{-2} \text{s}^{-1}$  for various energy ranges. Shown here are our results with an outer background radius of 16 Mpc. First Column: The energy range considered. Second: Outer radius of the background annulus. Third: Upper limits for the complete stack of 78 clusters. Fourth: Lowest flux upper limits found for the number of clusters producing the best limit in the stacking by variance method.

for the  $\gamma$ -ray emission from clusters by Huber et al. (2013), assuming that  $\pi^0$  decay is the main  $\gamma$ -ray emission source. Since our mass weighted luminosity limit is twice that of Huber et al. (2013), we place upper limits of the CR-to-thermal energy ratio of 8% as scaled to Huber et al. (2013), corresponding to a CR-to-thermal pressure ratio of  $P_{CR}/P_{Th} \simeq 4\%$ . These results confirm the recent claims (Huber et al. 2013; Prokhorov & Churazov 2014) that the CR energy and pressure contribute only marginally to the total energy and pressure of the intra-cluster gas. This reduces one uncertainty in estimating the hydrostatic cluster mass using thermal X-ray emission.

Moreover,  $\gamma$ -ray emission from galaxy clusters provides

an additional window to constrain the details of cluster formation. Large-scale cosmological simulations have successfully predicted the mass function of galaxy clusters. However, we lack additional constraints to test the details of these models because we generally observe only the final stages of the merging history. Since the cooling time of the hadronic CR component is longer than a Hubble time, the hadronic CR component essentially accumulates in clusters (e.g., Berezhinsky et al. 1997) so that the final  $\gamma$ -ray emission produced by the hadronic CRs depends on the full merger history. This should be compared to the CR electron-driven synchrotron radio emission – both are driven by the same shocks but the radio emission depends only on recent activity due to the short CR electron life times. Since cluster merger models predict that all clusters have experienced similar shocks during the assemblage history, the clusters with radio relics are considered an evolutionary stage of clusters because of the fast electron cooling time-scale.

Thus, we can compare the  $\gamma$ -ray flux constrained from a general cluster population with the radio flux from clusters with radio relics, because both the CR components are accelerated by the same shocks. While some model predicted  $\gamma$ -ray fluxes from clusters with radio halos are consistent with our limits (e.g., Kushnir et al. 2009), using a semi-analytical model, Vazza & Brüggen (2014) calculated the expected  $\gamma$ -ray emission from clusters with radio relics (arcs) that are evidence for shocks with Mach numbers of 2–4. Figure 3 (right) compares the predictions of Vazza & Brüggen (2014) (green diamonds) to the observed limits (arrows and horizontal lines), and, like Huber et al. (2013) our limits are well below the typical predictions. The problem can be more severe because there can be multiple mergers as a cluster forms. Several papers explored scenarios to resolve this discrepancy, including over-estimated Mach numbers from the radio data, lower energy deposition rates to the hadronic

CR component than in standard diffuse shock acceleration models, and reacceleration of electrons (e.g., Vazza & Brüggen 2014; Brunetti & Jones 2014; Zandanel et al. 2014).

This research has made use of the publicly available *Fermi*-LAT data. We thank the anonymous referee and G. Brunetti, T. A. Thompson, D. Kushnir, B. Katz, F. Zandanel, and J. Han for helpful comments.

## REFERENCES

- Abdo, A. A., Ackermann, M., Ajello, M., et al. 2009, *ApJ*, 707, 55  
 Abdo, A. A., Ackermann, M., Ajello, M., et al. 2009, *ApJ*, 699, 31  
 Ackermann, M., Ajello, M., Albert, A., et al. 2014, *ApJ*, 787, 18  
 Aleksić, J. et al. 2012, *A&A*, 541, 99  
 Amsler, C. et al. (Particle Data Group) 2008, *PL*, B667, 1  
 Arlen, R. et al. 2012, *ApJ*, 757, 123  
 Atwood, W. B. et al. 2009, *ApJ*, 697, 1071  
 Berezhinsky, V. S., Blasi, P., & Ptuskin, V. S. 1997, *ApJ*, 487, 529  
 Berrington, R. C. & Dermer, C. D. 2003, *ApJ*, 594, 709  
 Blackburne, J. A. & Kochanek, C. S. 2012, *ApJ*, 744, 76  
 Brunetti, G., & Jones, T. W. 2014, *International Journal of Modern Physics D*, 23, 30007  
 Dai, X., Kochanek, C. S., & Morgan, N. D. 2007, *ApJ*, 658, 917  
 Dai, X., Bregman, J. N., Kochanek, C. S., & Rasia, E. 2010, *ApJ*, 719, 119  
 Feretti, L., Giovannini, G., Govoni, F., & Murgia, M. 2012, *A&A Rev.*, 20, 54  
 Han, J., Frenk, C. S., Eke, V. R., et al. 2012, *MNRAS*, 427, 1651  
 Huber, B. et al. 2013, *A&A*, 560, 64  
 Huber, B. et al. 2012, *A&A*, 547, 102  
 Jeltema, T. E., Kehayias, J. & Profumo, S. 2009, *Physical Review D*, 80, 3005  
 Kochanek, C. S. et al. 2003, *ApJ*, 585, 161  
 Kravtsov, A. V. & Borgani, S. 2012, *ARA&A*, 50, 353  
 Kushnir, D., Katz, B., & Waxman, E. 2009, *JCAP*, 9, 24  
 Nolan, P. L., et al. 2012, *ApJS*, 199, 31  
 Pfrommer, C. & Enßlin, T. A. 2004, *A&A*, 413, 17  
 Pinzke, A. & Pfrommer, C. 2010, *MNRAS*, 409, 449  
 Prokhorov, D. A., & Churazov, E. M. 2014, *A&A*, 567, A93  
 Reiprich, T. H., & Böhringer, H. 2002, *ApJ*, 567, 716  
 Reimer, O., Pohl, M., Sreekumar, P., & Mattox, J. R. 2003, *ApJ*, 588, 155  
 Vazza, F. & Brüggen, M. 2014, *MNRAS*, 437, 2291  
 Völk, H. J., Aharonian, F. A., & Breitschwerdt, D. 1996, *Space Sci. Rev.*, 75, 279  
 Zandanel, F., & Ando, S. 2014, *MNRAS*, 440, 663  
 Zandanel, F., Pfrommer, C., & Prada, F. 2014, *MNRAS*, 438, 124